Journal of Biomedical Optics

BiomedicalOptics.SPIEDigitalLibrary.org

Sequential weighted Wiener estimation for extraction of key tissue parameters in color imaging: a phantom study

Shuo Chen
Xiaoqian Lin
Caigang Zhu
Quan Liu

SPIE.

Sequential weighted Wiener estimation for extraction of key tissue parameters in color imaging: a phantom study

Shuo Chen, Xiaoqian Lin, Caigang Zhu, and Quan Liu*
Nanyang Technological University, School of Chemical and Biomedical Engineering, Division of Bioengineering, 70 Nanyang Drive, Singapore 637457, Singapore

Abstract. Key tissue parameters, e.g., total hemoglobin concentration and tissue oxygenation, are important biomarkers in clinical diagnosis for various diseases. Although point measurement techniques based on diffuse reflectance spectroscopy can accurately recover these tissue parameters, they are not suitable for the examination of a large tissue region due to slow data acquisition. The previous imaging studies have shown that hemoglobin concentration and oxygenation can be estimated from color measurements with the assumption of known scattering properties, which is impractical in clinical applications. To overcome this limitation and speed-up image processing, we propose a method of sequential weighted Wiener estimation (WE) to quickly extract key tissue parameters, including total hemoglobin concentration (C_{tHb}), hemoglobin oxygenation (StO_2), scatterer density (α), and scattering power (β), from wide-band color measurements. This method takes advantage of the fact that each parameter is sensitive to the color measurements in a different way and attempts to maximize the contribution of those color measurements likely to generate correct results in WE. The method was evaluated on skin phantoms with varying C_{tHb}, StO_2, and scattering properties. The results demonstrate excellent agreement between the estimated tissue parameters and the corresponding reference values. Compared with traditional WE, the sequential weighted WE shows significant improvement in the estimation accuracy. This method could be used to monitor tissue parameters in an imaging setup in real time. *© 2014 Society of Photo-Optical Instrumentation Engineers (SPIE)* [DOI: 10.1117/1.JBO.19.12.127001]

Keywords: biomedical optical imaging; color imaging; Wiener estimation; tissue characterization.

Paper 140496RR received Jul. 31, 2014; accepted for publication Nov. 4, 2014; published online Dec. 2, 2014.

1 Introduction

Key tissue parameters, e.g., total hemoglobin concentration and tissue oxygenation, are important biomarkers in clinical diagnosis for various diseases.[1] The previous studies have shown that diffuse reflectance spectroscopy can be used to accurately recover these parameters noninvasively using different methods, such as Monte Carlo-based inverse model,[2] diffusion theory-based model,[3] and the look-up table method.[4] However, the common disadvantage of traditional diffuse reflectance spectroscopy is slow data acquisition when multiple locations need to be measured.[5] This is attributed to the employment of fiber-optic probes in traditional diffuse reflectance spectroscopy, which can only perform point measurements. Slow data acquisition prohibits the use of diffuse reflectance spectroscopy in those applications in which the observation of fast changing phenomena is required.

Several spectral imaging techniques are developed to speed up the data acquisition. Multispectral imaging[6–8] captures image data at certain wavelengths using specific filters or instruments that are sensitive to particular wavelengths instead of the entire spectrum. The advantage of this technique is that both the spectral and spatial information can be recorded simultaneously.[9] However, the data acquisition is time consuming when high spectral resolution is required. This limitation originates from the employment of a wavelength selection/dispersion device in most imaging setups, for which information at only one or a couple of wavelengths can be collected in one measurement. Snapshot hyperspectral imaging is a technique in which both the spatial and spectral information are acquired simultaneously in a snap shot[10] but in a coded manner. The key idea in snapshot hyperspectral imaging is that hyperspectral images can be captured all at once on a two-dimensional detector array. The disadvantage of snapshot hyperspectral imaging techniques is that data postprocessing is slow when the required spectral resolution is high. In addition, a large detector array is needed to properly sample a sufficient number of voxels and those large detector arrays are usually expensive. To overcome this limitation, spectral imaging can be realized by spectral reconstruction from wide-band measurements such as color imaging measurements, in which a method capable of fast and accurate spectral reconstruction is critical. Various methods have been explored to reconstruct diffuse reflectance spectra from wide-band measurements, which includes pseudo-inverse,[11] finite-dimensional modeling,[12] and Wiener estimation (WE).[13] Our previous study[5] has shown that diffuse reflectance spectra can be accurately recovered from *in vivo* color measurements on human skin. Therefore, it may be possible to directly derive tissue parameters from wide-band measurements.

Multiple early studies[14,15] have shown that hemoglobin concentration and oxygenation in tissue phantoms with known scattering properties can be estimated from color measurements in R(Red), G (Green), B(Blue) channels using a method involving Monte Carlo modeling and multiple steps of regression analysis. However, the scattering properties of tissues carry important physiological information,[16] which are typically unknown and can vary

*Address all correspondence to: Quan Liu, E-mail: quanliu@ntu.edu.sg

0091-3286/2014/$25.00 © 2014 SPIE

significantly from one subject to another. To our best knowledge, there is no previous study in which both absorption and scattering properties are directly estimated from wide-band measurements in a tissue model with varying or unknown scattering properties.

In this study, we reported a method of sequential weighted WE to directly extract total hemoglobin concentration (C_{tHb}), hemoglobin oxygenation (StO_2), scatterer density (α), and scattering power (β) from wide-band measurements. This method takes advantage of the fact that each parameter is sensitive to the color measurements to a different degree and attempts to maximize the contribution of those color measurements that are more likely to generate correct results in the process of WE. The method was evaluated on tissue phantoms with varying C_{tHb}, StO_2, and scattering properties to mimic human skin, in which a 3-charge coupled device (CCD) camera was used to capture the wide-band color measurements from the tissue phantoms. The results demonstrate excellent agreement between the estimated tissue parameters and the corresponding reference values. Compared with the traditional WE, the method of sequential weighted WE shows significant improvement, especially for hemoglobin oxygenation estimation. This method possesses great potential in the noninvasive and real-time monitoring of tissue parameters in an imaging setup to investigate fast changing phenomena.

2 Materials and Methods

In this study, tissue phantoms with varying absorption, scattering, and oxygenation were used to mimic the human skin. Both traditional WE and sequential weighted WE were tested to extract tissue parameters, including the total hemoglobin concentration (C_{tHb}), hemoglobin oxygenation (StO_2), scatterer density (α), and scattering power (β). The leave-one-out method was used for cross validation and the genetic algorithm was utilized to find the optimal combination of coefficients. All the postprocessing steps, including the traditional WE, sequential weighted WE, leave-one-out method, and genetic algorithm, were coded and run in Matlab (R2011b, MathWorks, Natick, Massachusetts). The details in each step are described as follows.

2.1 *System Information*

In this study, all the data were measured by the system shown in Fig. 1, which consisted of a white light source (UHP-Mic-LED-White, Prizmatix, Givat-Shmuel, Illinois), a 3-CCD (AT-200 GE, JAI, San Jose, California), a magnetic stirrer (97042-596, VWR, Radnor, Pennsylvania), and two linear polarizers (LPVISE100-A, Thorlabs, Newton, New Jersey). White light passed through the first linear polarizer, which was aligned such that its direction of polarization was parallel to the source-sample-detector plane. The illumination light was delivered at a fixed angle of 45 deg onto a sample to avoid the collection of specular reflectance.[17] The second linear polarizer was put in front of the 3-CCD in order to acquire signals with two different polarization directions (parallel or perpendicular to the incident polarization). The signal detected with parallel polarization contained contributions from both the superficial and deep regions inside the phantom, in which photons responsible for contribution from the superficial are mostly scattered only a single or a few times.[18,19] Therefore, the signal detected with parallel polarization was expected to be sensitive to the scattering properties of the phantoms thus, in turn, to the scatterer density (α) and scattering power (β). By contrast, the signal detected with perpendicular polarization contained only light from deep regions inside the phantom, which was expected to be sensitive to the absorption properties of the phantoms due to the long optical path length and to total hemoglobin concentration (C_{tHb}) and hemoglobin oxygenation (StO_2). The sample was viewed by the camera right above, along the normal axis of the sample surface. A computer was connected to the camera to acquire the images of the sample, which contained the wide-band color measurements. Among these tissue parameters, hemoglobin concentration and oxygen saturation together determine the absorption coefficient spectrum according to Beer's law, whereas the scattering amplitude and scattering power together determine the reduced scattering coefficient μ_s' for the whole visible spectrum (λ) by the following empirical equation:[20,21]

$$\mu_s'(\lambda) = \alpha\lambda^{-\beta}. \tag{1}$$

The spectra of absorption and scattering coefficients together with the configuration of optical measurements determine the diffuse reflectance spectrum. After passing through the RGB (i.e., Red, Green, and Blue) filters, the diffuse reflectance spectrum is transformed to RGB values, as shown in Eq. (2):

$$C = FS, \tag{2}$$

where C is the RGB responses, F represents the transmission spectra of RGB filters, and S is the diffuse reflectance spectrum. Therefore, the RGB responses and their ratios are determined by these tissue parameters and, therefore, contain the information of all the tissue parameters. A pH meter and thermometer (HI 9024, Sigma-Aldrich, St. Louis, Missouri) and a dissolved oxygen meter (HI 9142, Sigma-Aldrich, St. Louis, Missouri) were used to measure the pH value, temperature, and oxygen level in the phantom sample, respectively, which were used to derive hemoglobin oxygenation. The relative emission spectrum of the white light source, the relative spectral response of the 3-CCD, and the transmittance of the polarizers are shown in Fig. 2.

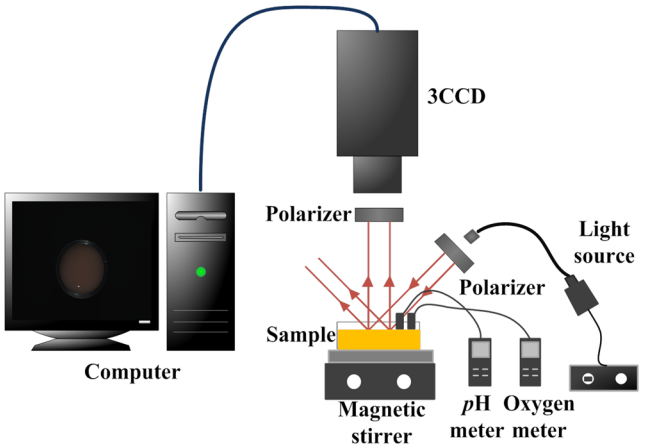

Fig. 1 Schematic of the color imaging system with devices measuring pH and dissolved oxygen in the sample. The red lines with arrows represent light flow.

2.2 *Phantom Preparation*

The optical properties of tissue phantoms were selected to mimic human skin, in which hemoglobin served as the absorber and polystyrene spheres served as scatterers.

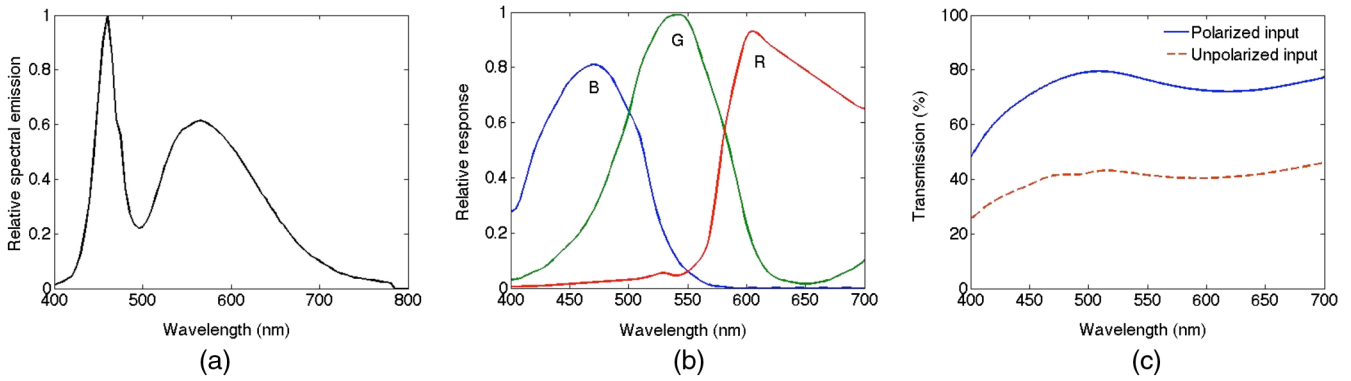

Fig. 2 (a) Relative emission spectrum of white light source, (b) relative spectral response of the 3-CCD, and (c) transmittance of the polarizer.

In total, 162 liquid phantoms with three different hemoglobin concentrations, polystyrene spheres with two different scatterer sizes and three different volume concentrations, and nine different hemoglobin oxygenations were measured. The three concentrations of hemoglobin (H0267, Sigma-Aldrich, St. Louis, Missouri) were 3.9, 19.4, and 38.8 μM, which correspond to absorption coefficients of 2.3, 11.5, and 23 cm^{-1} at 413 nm. The volume concentrations of polystyrene spheres with a 1-μm diameter (07310-1, Polysciences, Warrington, Pennsylvania) were adjusted to achieve the scattering coefficients of 54.8, 109.6, and 253.5 cm^{-1} at 550 nm. The volume concentrations of polystyrene spheres with a 0.5-μm diameter (07307-15, Polysciences, Warrington, Pennsylvania) were adjusted to achieve the scattering coefficients of 55.0, 110.0, and 256.6 cm^{-1} at 550 nm. The optical properties of the skin phantoms used in this study were extracted from *in vivo* skin studies[22–24] and *in vitro* skin studies,[25–27] in which the subjects were mostly Caucasians. A phosphate buffer with a pH of 6.0 was used as the solvent in the phantoms to keep a constant pH value, which maintained the relation between the measured oxygen tension and hemoglobin oxygenation as approximately unchanged when the temperature was fixed.[1] Hemoglobin oxygenation was varied by adding 5 mg/ml yeast (Dry Baker's Yeast, saf-instant, Marcq-en-Baroeul, Cedex, France) to remove oxygen from hemoglobin. The recorded hemoglobin oxygenation values ranged from 10% to 90% with an interval of 10%. The phantoms were consistently stirred at a moderate speed on top of the magnetic stirrer during measurements to maintain a uniform distribution of oxygenation and scatterer distribution. The dissolved oxygen meter was used to monitor oxygen concentration in the phantoms. The measured oxygen concentration was converted to hemoglobin oxygenation by applying Henry's law[28] and Kelman's equation[29,30] with the required parameters, i.e., pH and temperature values measured by the pH meter and the thermometer. It was found that the pH and temperature of the phantoms were maintained at ~6.0 and 20°C, respectively, during the measurements.

2.3 *Data Analysis*

2.3.1 *Sequential weighted WE*

In traditional WE, when ignoring the noise term, the Wiener matrix is formulated as

$$W = E[sc^{\mathrm{T}}][E[cc^{\mathrm{T}}]]^{-1}, \tag{3}$$

where the superscript "T" represents the matrix transpose, the superscript "−1" represents the matrix inverse, $E[]$ represents the ensemble average, s represents the tissue parameters, and c represents the wide-band measurements. More details for traditional WE have been reported elsewhere.[31] In the weighted WE that we developed, the ensemble average is replaced by the weighted average as shown in Eq. (4):

$$W = \sum_{i=1}^{n} w_i s_i c_i^T \sum_{j=1}^{n} (w_j c_j c_j^T)^{-1}, \tag{4}$$

where w_i or w_j is the weight for the i'th or j'th set of calibration data. This weight is calculated according to the following equation:

$$w_i = \frac{D_i^m}{\sum_{i=1}^{n} D_i^m}, \tag{5}$$

where D_i is the similarity between the tissue parameter value estimated from the test data and the corresponding parameter value in the i'th set of tissue parameters in the calibration data and m is the power to adjust the contribution of D_i. The similarity D_i is calculated according to Eq. (6):

$$D_i = \frac{d_i^{-1}}{\sum_{i=1}^{n} d_i^{-1}}, \tag{6}$$

where d_i denotes the difference between the tissue parameter value estimated from the test data and the corresponding parameter value in the i'th set of tissue parameters in the calibration data and m is the power to adjust the contribution of d_i. When multiple estimated tissue parameters need to be included in the weighting scheme, the corresponding similarity values will be calculated separately according to Eq. (6) and then averaged to yield a single similarity value. The accuracy of the estimation can be improved by using a large number of calibration data highly similar to the test data set. According to Eqs. (5) and (6), any calibration data with a set of tissue parameter values very different from the test data would yield a tiny weight, which makes a nearly negligible contribution to the weighted Wiener matrix by Eq. (4). According to the same equations, a larger m generates a more effective calibration data set, which is more similar to the test data set, than a smaller m does. However, if m becomes too large, the weight can be

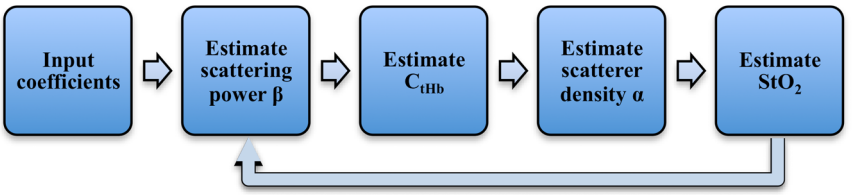

Fig. 3 Schematic of sequential weighted Wiener estimation (WE).

very small not only for those calibration data very different from the test data but also for those calibration data moderately similar to the test data by Eqs. (5) and (6). As a result, the effective calibration data will be much less because only those very similar to the test data are retained. Such a small set of calibration data is likely to yield large errors in estimation when the calibration data or the test data contain measurement uncertainty or noises. Therefore, the adjustment of m is the tradeoff between the population size of the effective calibration data and the similarity between the calibration data set and the test data set, when the full calibration data set is fixed. The value of m was fixed at 5 in this study to achieve the tradeoff. According to Eq. (4) to Eq. (6), the summation of w_i is 1, and the contribution of a set of calibration data to the Wiener matrix is proportional to the similarity between the estimated tissue parameters in the test data set and the i'th set of tissue parameters in the calibration data.

The schematic of the sequential weighted WE is shown in Fig. 3. This method consists of multiple steps of estimation that can be run iteratively, in which the parameters in the order of estimation are the scattering power (β), the total hemoglobin concentration (C_{tHb}), the scatterer density (α), and hemoglobin oxygenation (StO_2). The estimation error of each individual parameter when using traditional WE decreases with this order in the calibration stage; therefore, this order will prevent the early estimation error from propagating to the later estimation. In the first step, the scattering power β is extracted using a traditional WE method. Then, C_{tHb} is estimated using the weighted WE as in Eq. (4) and the weights are calculated using Eqs. (5) and (6) according to the difference between the β value estimated from the test data and the β values in the calibration data. After that, α is estimated using the weighted WE as in Eq. (4) and the weights are calculated using Eqs. (5) and (6) according to the difference between C_{tHb} and β values estimated from the test data and these values in the calibration data. Finally, StO_2 is estimated using the weighted WE as in Eq. (4) and the weights are calculated according to the difference between C_{tHb}, α, and β values estimated from the test data and these values in the calibration data. This completes one loop in the sequential weighted WE. If the estimated results are not satisfactory, the loop can be run again, in which β will be calculated again according to the weights calculated according to the similarity between C_{tHb}, StO_2 and α values estimated from the test data in the first loop and those values in the calibration data. All the steps can be repeated iteratively until the estimated results are acceptable.

2.3.2 *Leave-one-out method, genetic algorithm and evaluation criterion*

The leave-one-out method[32] was used for cross validation. In this strategy, data measured from one tissue phantom are used for testing and data measured from other tissue phantoms are used for calibration. Then a new tissue phantom is selected for testing and the procedure is repeated until all the tissue phantoms have been tested.

Because the ratios of wide-band measurements contained important information about hemoglobin,[33,34] we examined both the absolute values of wide-band measurements and their ratios. These two sets of data were named jointly as coefficients in Table 1. A genetic algorithm was used to find the optimal combination of the coefficients for the estimation of each tissue parameter. The optimization methodology proceeded in the following manner. First, a population of coefficient combination was initialized randomly. Second, the traditional WE (for comparison) or sequential weighted WE was applied to extract the tissue parameters and the accuracy of the recovered tissue parameters was evaluated. The accuracy was quantified according to the relative root mean square error (RMSE) calculated from Eq. (7). Third, a new population of coefficient combination was generated according to the accuracy of the recovered tissue parameters, in which the coefficient combination yielding a higher accuracy was more likely to become the parent of the new population. The crossover rate was 0.9 and the mutation rate was 0.1. The second and third steps were repeated

Table 1 Coefficients for estimation of tissue parameters.[a]

Indices	Coefficients
1 ~ 12	$R_{\parallel}$, $G_{\parallel}$, $B_{\parallel}$, $R_{\perp}$, $G_{\perp}$, $B_{\perp}$, R_{sum}, G_{sum}, B_{sum}, R_{sub}, G_{sub}, B_{sub}
13 ~ 24	$R_{\parallel}/(R_{\parallel}+G_{\parallel}+B_{\parallel})$, $G_{\parallel}/(R_{\parallel}+G_{\parallel}+B_{\parallel})$, $B_{\parallel}/(R_{\parallel}+G_{\parallel}+B_{\parallel})$, $R_{\perp}/(R_{\perp}+G_{\perp}+B_{\perp})$, $G_{\perp}/(R_{\perp}+G_{\perp}+B_{\perp})$, $B_{\perp}/(R_{\perp}+G_{\perp}+B_{\perp})$, $R_{sum}/(R_{sum}+G_{sum}+B_{sum})$, $G_{sum}/(R_{sum}+G_{sum}+B_{sum})$, $B_{sum}/(R_{sum}+G_{sum}+B_{sum})$, $R_{sub}/(R_{sub}+G_{sub}+B_{sub})$, $G_{sub}/(R_{sub}+G_{sub}+B_{sub})$, $B_{sub}/(R_{sub}+G_{sub}+B_{sub})$
25 ~ 36	$R_{\parallel}/G_{\parallel}$, $R_{\parallel}/B_{\parallel}$, $G_{\parallel}/R_{\parallel}$, $G_{\parallel}/B_{\parallel}$, $B_{\parallel}/R_{\parallel}$, $B_{\parallel}/G_{\parallel}$, $R_{\perp}/G_{\perp}$, $R_{\perp}/B_{\perp}$, $G_{\perp}/R_{\perp}$, $G_{\perp}/B_{\perp}$, $B_{\perp}/R_{\perp}$, $B_{\perp}/G_{\perp}$
37 ~ 48	R_{sum}/G_{sum}, R_{sum}/B_{sum}, G_{sum}/R_{sum}, G_{sum}/B_{sum}, B_{sum}/R_{sum}, B_{sum}/G_{sum}, R_{sub}/G_{sub}, R_{sub}/B_{sub}, G_{sub}/R_{sub}, G_{sub}/B_{sub}, B_{sub}/R_{sub}, B_{sub}/G_{sub}

[a]R, red value; G, green value; B, blue value; ||, light with parallel polarization; ⊥, light with perpendicular polarization; sum, || + ⊥; sub, || − ⊥.

iteratively until an optimized combination of coefficient was found:

$$\text{Relative RMSE} = \sqrt{\frac{\sum_{i=1}^{n}\left(\frac{i\text{th estimated parameter} - i\text{th reference parameter}}{i\text{th reference parameter}}\right)^2}{n}}. \quad (7)$$

3 Results

Table 2 shows the relative RMSEs in the parameters estimated using traditional WE and the sequential weighted WE relative to the reference values. Out of four parameters estimated, i.e., C_{tHb}, StO_2, scatterer density α, and scattering power β, the relative RMSEs increase from the lowest to the highest for traditional WE in the order of β, C_{tHb}, α, and StO_2, and the sequential weighted WE performs estimations in the same sequence as shown in Fig. 3. The first weighted WE denotes the sequential weighted WE with only one iteration and the second weighted WE denotes the sequential weighted WE with two iterations. The relative RMSEs in estimated tissue parameters after the first-iteration weighted WE are 71.0%, 22.2%, 19.9% and 92.7% of those after traditional WE for C_{tHb}, StO_2, α, and β, respectively. The relative RMSEs after the second-iteration weighted WE are 24.1%, 96.5%, 94.4% and 49.3% of those after the first weighted WE for the same parameters. The decreases in the relative RMSEs of parameters indicate that the sequential weighted WE improves the estimation as the number of iteration increases.

Table 2 Relative RMSEs in the parameters estimated using traditional WE and sequential weighted WE relative to the reference values.

	Traditional WE	First-iteration weighted WE	Second-iteration weighted WE
Relative RMSE in C_{tHb}	0.1681	0.1193	0.0287
Relative RMSE in StO_2	1.2712	0.2825	0.2726
Relative RMSE in α	0.2517	0.0501	0.0473
Relative RMSE in β	0.0151	0.0140	0.0060

Figure 4 graphically shows the comparison between estimated parameters and reference parameters in the traditional WE and sequential weighted WE. It is observed that the markers representing the weighted WE stay much more packed and closer to the ideal lines than those representing the traditional WE, which suggests that the weighted WE, especially after two iterations, is more effective in the quantification of these parameters.

The best combination of coefficients for estimating C_{tHb}, StO_2, α, and β in the traditional WE, the first-iteration weighted WE, and the second-iteration weighted WE are shown in

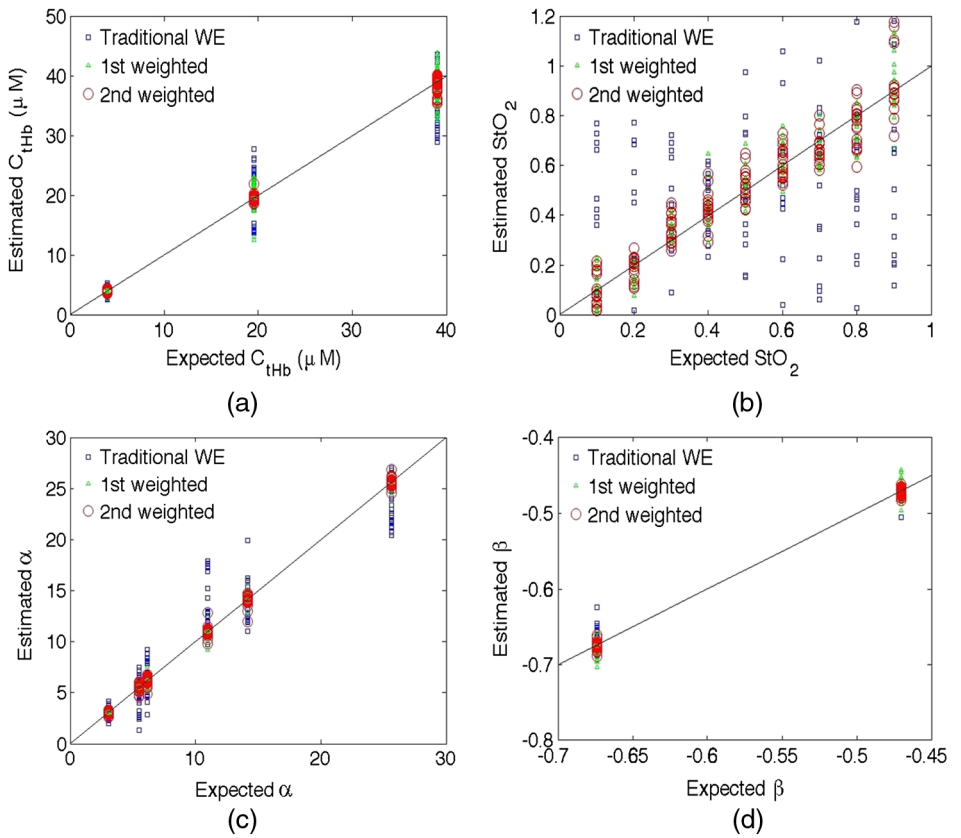

Fig. 4 (a) Total hemoglobin concentration C_{tHb}, (b) hemoglobin oxygenation StO_2, (c) scatterer density α, and (d) scattering power β estimated using the traditional WE and weighted WE as a function of the expected value. The legend "1st weighted" means the result after the first iteration of weighted WE and the legend "2nd weighted" means the result after the second iteration of weighted WE.

Table 3 The best combination of coefficients for estimating C_{tHb} StO_2, α and β in traditional WE, the first-iteration weighted WE and the second-iteration weighted WE.

	Traditional WE	First-iteration weighted WE	Second-iteration weighted WE
C_{tHb}	$B_{\parallel}$, $R_{\perp}$, R_{sum}, $R_{\parallel}/(R_{\parallel}+G_{\parallel}+B_{\parallel})$, $R_{sum}/(R_{sum}+G_{sum}+B_{sum})$, $G_{sum}/(R_{sum}+G_{sum}+B_{sum})$, $G_{sub}/(R_{sub}+G_{sub}+B_{sub})$, $B_{\parallel}/G_{\parallel}$, G_{sum}/R_{sum}, R_{sub}/G_{sub}, B_{sub}/G_{sub}	$R_{\parallel}$, $B_{\parallel}$, $R_{\perp}/(R_{\perp}+G_{\perp}+B_{\perp})$, $R_{\perp}/G_{\perp}$, $R_{\perp}/B_{\perp}$, $G_{\perp}/R_{\perp}$, $G_{\perp}/B_{\perp}$, $B_{\perp}/R_{\perp}$, R_{sum}/B_{sum}, B_{sum}/G_{sum}	$R_{\perp}/(R_{\perp}+G_{\perp}+B_{\perp})$, $G_{\perp}/(R_{\perp}+G_{\perp}+B_{\perp})$, $R_{\perp}/G_{\perp}$
StO_2	$R_{\parallel}$, $R_{\perp}$, R_{sum}, B_{sum}, R_{sub}, B_{sub}, $R_{\parallel}/(R_{\parallel}+G_{\parallel}+B_{\parallel})$, $B_{sum}/(R_{sum}+G_{sum}+B_{sum})$, $G_{\parallel}/R_{\parallel}$, $G_{\perp}/B_{\perp}$	R_{sum}, B_{sum}, $R_{sum}/(R_{sum}+G_{sum}+B_{sum})$, $G_{sum}/(R_{sum}+G_{sum}+B_{sum})$, $B_{sum}/(R_{sum}+G_{sum}+B_{sum})$, G_{sum}/R_{sum}, B_{sum}/R_{sum}	B_{sum}, $R_{sum}/(R_{sum}+G_{sum}+B_{sum})$, $G_{\perp}/R_{\perp}$, G_{sum}/B_{sum}
α	$R_{\perp}$, B_{sum}, G_{sub}, $G_{\parallel}/(R_{\parallel}+G_{\parallel}+B_{\parallel})$, $G_{\perp}/(R_{\perp}+G_{\perp}+B_{\perp})$, $B_{sub}/(R_{sub}+G_{sub}+B_{sub})$, $R_{\parallel}/G_{\parallel}$, R_{sum}/G_{sum}, G_{sum}/B_{sum}, R_{sub}/B_{sub}, G_{sub}/B_{sub}	R_{sum}, B_{sum}, $R_{\parallel}/(R_{\parallel}+G_{\parallel}+B_{\parallel})$, $B_{\parallel}/(R_{\parallel}+G_{\parallel}+B_{\parallel})$, $R_{\perp}/(R_{\perp}+G_{\perp}+B_{\perp})$, $G_{sum}/(R_{sum}+G_{sum}+B_{sum})$, $R_{\parallel}/G_{\parallel}$, $B_{\parallel}/G_{\parallel}$, B_{sum}/R_{sum}, B_{sum}/G_{sum}	$B_{\parallel}$, $R_{\perp}$, G_{sum}, B_{sum}, $R_{\perp}/(R_{\perp}+G_{\perp}+B_{\perp})$, $G_{\perp}/(R_{\perp}+G_{\perp}+B_{\perp})$, $R_{sum}/(R_{sum}+G_{sum}+B_{sum})$, $G_{sub}/(R_{sub}+G_{sub}+B_{sub})$, $G_{sub}/(R_{sub}+G_{sub}+B_{sub})$, $R_{\perp}/G_{\perp}$, $G_{\perp}/R_{\perp}$, B_{sum}/R_{sum}, R_{sub}/G_{sub}
β	R_{sum}, R_{sub}, $R_{\perp}/(R_{\perp}+G_{\perp}+B_{\perp})$, $R_{sum}/(R_{sum}+G_{sum}+B_{sum})$, $B_{sum}/(R_{sum}+G_{sum}+B_{sum})$, $R_{sub}/(R_{sub}+G_{sub}+B_{sub})$, $R_{sub}/(R_{sub}+G_{sub}+B_{sub})$, $G_{sub}/(R_{sub}+G_{sub}+B_{sub})$, $B_{sub}/(R_{sub}+G_{sub}+B_{sub})$, G_{sub}/R_{sub}, G_{sub}/B_{sub}, B_{sub}/R_{sub}, B_{sub}/G_{sub}	$R_{\parallel}$, $G_{\parallel}/(R_{\parallel}+G_{\parallel}+B_{\parallel})$, $G_{sum}/(R_{sum}+G_{sum}+B_{sum})$, $B_{sub}/(R_{sub}+G_{sub}+B_{sub})$, $B_{sub}/(R_{sub}+G_{sub}+B_{sub})$, $R_{\parallel}/G_{\parallel}$, $R_{\perp}/G_{\perp}$, R_{sum}/G_{sum}, R_{sum}/B_{sum}, G_{sum}/R_{sum}, R_{sub}/G_{sub}, G_{sub}/B_{sub}	$R_{\parallel}$, $R_{\parallel}/(R_{\parallel}+G_{\parallel}+B_{\parallel})$, $B_{\parallel}/(R_{\parallel}+G_{\parallel}+B_{\parallel})$, $B_{\perp}/(R_{\perp}+G_{\perp}+B_{\perp})$, $B_{sum}/(R_{sum}+G_{sum}+B_{sum})$, $G_{sub}/(R_{sub}+G_{sub}+B_{sub})$, $G_{sub}/(R_{sub}+G_{sub}+B_{sub})$, $G_{\parallel}/R_{\parallel}$, $G_{\parallel}/B_{\parallel}$, R_{sub}/G_{sub}, B_{sub}/R_{sub}, B_{sub}/G_{sub}

Table 3. It is interesting to observe that not only the best combination but also the number of coefficients in the best combination change from the traditional WE to the weighted WE as well as from the first iteration to the second iteration in the weighted WE.

4 Discussion

According to Table 2 and Fig. 4, all the estimated parameters show significant improvement when using the sequential weighted WE. The traditional WE fails to recover the StO_2, whereas the sequential weighted WE shows good performance for the recovery of StO_2. The improvement can be attributed to the optimal selection of the calibration data set, in which a more appropriate Wiener matrix is created compared with the traditional WE. In addition, with the increasing number of iterations in the sequential weighted WE, all the estimated parameters show improved accuracies. This is due to the better choices of weights used in Eqs. (4) to (6), i.e., more contribution from the calibration data with a higher similarity to the test data, which means a more appropriate Wiener matrix can be created. However, more iterations require more computation time, thus a trade-off is needed between the estimation accuracy and the time cost in a clinical application.

In all the data shown up to this point, the similarity values calculated separately for each parameter according to Eq. (6) were averaged to represent the similarity of the multiple parameters in each set of data. We also evaluated the possibility of using the multiplication of individual similarity values instead

Table 4 Relative RMSEs in the parameters estimated using sequential weighted WE based on averaging and multiplication for the similarity indicator of multiple parameters.

	First-iteration weighted WE (averaging)	Second-iteration weighted WE (averaging)	First-iteration weighted WE (multiplication)	Second-iteration weighted WE (multiplication)
Relative RMSE in C_{tHb}	0.1193	0.0287	0.1193	0.0151
Relative RMSE in StO_2	0.2825	0.2726	0.2978	0.3070
Relative RMSE in α	0.0501	0.0473	0.0430	0.0421
Relative RMSE in β	0.0140	0.0060	0.0065	0.0030

of the averaging of them to generate a single similarity indicator for the multiple parameters in each set of data as shown in Table 4, in which multiplication was found to yield a faster convergence than averaging. The results in Table 4 show significant improvement on the estimation of C_{tHb} and β, a slight improvement in the estimation of α, and a slight degradation in StO_2 estimation accuracy.

According to Table 3, all the combination of parameters contains ratio values of wide-band measurements, which confirms the importance of ratio values for the recovery of all tissue parameters. However, there is no obvious preference in the polarization state of light and/or specific ratio values for the recovery of any individual tissue parameter. The possible reason is that although a certain coefficient is more important for a given tissue parameter, information from other coefficients is still needed for accurate estimation in this particular imaging setup. For example, the scattering properties including α and β are generally considered to be more sensitive to the measurements in parallel polarization that involves most contribution from the shallow sample volume. In principle, the measurements in perpendicular polarization should not appear in the optimal combination of coefficients for estimating the scattering properties. However, the small detector, which is determined by the pixel size of the camera in this imaging setup, could break this principle since a small detector also preferentially detects signals from the shallow sample volume. As a result, multiple coefficients involving the measurements of perpendicular polarization are also included in the optimal combination for estimating the scattering properties, α and β, in Table 3. Interestingly, only the measurements of perpendicular polarization or the sum of measurements in both polarizations show up in the optimal combination for estimating C_{tHb} and StO_2. The excellent performance of the sequential weighted WE can be attributed to two factors. One factor is that the proposed method based on WE takes advantage of prior information about the samples contained in the Wiener matrix.[35] The Wiener matrix is created in the calibration stage, in which the tissue parameters measured from similar samples are used and associated with color measurements. The other factor is that the sequentially introduced weights yield an optimal calibration data set for each sample, thus a more appropriate Wiener matrix is created. This is also an advantage compared with the previous approach for the same problem,[15] in which fixed scattering coefficients and anisotropy factors were used. Because the color measurements are influenced jointly by all tissue parameters, the estimation of one particular tissue parameter, especially StO_2, which is essentially done by comparison between the test data and the similar data in the calibration data set, can be easily hindered by a small perturbation or error in other tissue parameters. In this situation, the calibration data set created by the weighting step in the sequential weighted WE, which is more similar to the test data than the raw calibration data set, will yield a Wiener matrix that is more robust to perturbation in the color measurements or other tissue parameters. Moreover, it is adaptive to different test data. Compared with the sequential weighted WE, the traditional WE only needs to create the Wiener matrix once. Therefore, the computing time for the sequential weighted WE is around 50 times of that for the traditional WE in this study. However, this problem could be solved by the prior calculation of the weighted Wiener matrix, which can be stored in a database according to the corresponding weights. When certain weights appear, the Wiener matrix can be directly retrieved from the database and the computing time can be reduced dramatically.

Although the use of the calibration data set is a potential limitation of this method, it should be pointed out that the calibration data set is often available in most biomedical applications. This fact has been utilized in many earlier researches in medical diagnostics.[36,37] However, when a totally new system (with a new light source and/or a new color CCD) is used, the instrument to instrument difference can degrade the estimation accuracy, since the calibration data set and the test data set were measured by using different systems. The problem can be solved by converting the RGB values into the CIE (International Commission on Illumination) XYZ color space. The CIE XYZ color space is a device-independent color space.[38] The RGB values are transformed to CIE XYZ values by a transform matrix T as shown in Eq. (8):

$$\begin{bmatrix} X \\ Y \\ Z \end{bmatrix} = T \begin{bmatrix} R \\ G \\ B \end{bmatrix}. \tag{8}$$

The transformation matrix T is dependent on the imaging system, which can be determined according to the measurements of a standard color chart using the imaging system. The standard color chart is supplied commercially with the corresponding CIE XYZ values. When the imaging system is changed, one just needs to obtain a new transformation matrix T by measuring the standard color chart again. The new transformation matrix will then be used to convert all color measurements from other samples to the CIE XYZ values; this process is device independent, thus it would be consistent regardless of the imaging system. This method will solve the problem of switching the imaging system from one to another. The detailed information of this method can be found in a published paper.[14] For color reading variation due to factors other than the system, for example, the slight variation in the imaging distance or angle, a single standard measurement can be applied to simplify the calibration step. The standard measurements are the measurements of a diffuse reflectance standard by using the current system and the new system. The color response can be corrected using Eq. (9):

$$C' = C_{new} \frac{S_{cur}}{S_{new}}, \tag{9}$$

where C' is the corrected color measurements, C_{new} is the color measurements from the new system, and S_{cur} and S_{new} are the standard measurements using the current system and new system, respectively. After the correction, the calibration data set acquired by the current system can be still used and the original Wiener matrix would remain effective. Another estimation degradation factor from ambient light could be reduced by subtracting the background measurement from any sample measurement. For every sample measurement, a subsequent background measurement was taken immediately and then subtracted from the sample measurement, which has been shown effective in reducing the influence of ambient light.

Compared with diffuse reflectance spectroscopy-based methods, the results for traditional WE do look worse. However, the sequential weighted WE improved the relative RMSEs over traditional WE by an average of 4.6 fold, ranging from 0.6% to 27%. The relative RMSEs generated by the sequential weighted

WE are comparable to the typical performance of diffuse reflectance spectroscopy-based methods,[2,4,39,40] in which the relative RMSEs were approximately ranged from 1% to 15%. Although optical spectroscopy for tissue characterization in a point measurement setup has been investigated intensively to derive key tissue parameters for a couple of decades, color imaging for the same purpose has not been fully explored, which is evident from the limited number of relevant publications. Compared to the point measurement setup, we anticipate that our method will be advantageous in the speed of data acquisition when employed for extraction of tissue parameters in a large field of view and high spatial resolution. In addition, the color imaging setup acquires images much faster than those more expensive spectral imaging setups. Our method requires only one color image based on which tissue parameters at each pixel can be reconstructed. Therefore, it may allow noninvasive and real-time monitoring of tissue parameters in a large tissue area to investigate fast changing phenomena.

The proposed method can be used in the clinical setting for various applications such as the assessment of skin viability. This study is a pilot study to verify the feasibility of tissue parameter extraction from RGB responses and their ratios and the efficiency of the proposed estimation algorithm. Therefore, a simplified phantom model was selected. Based on the feasibility of this study, the calibration data may need to be obtained from a more realistic tissue phantom model in clinical applications. For example, a series of two-layered skin phantoms including melanin in the epidermis with a range of epidermal thicknesses and optical properties in both layers will yield a better set of calibration data for clinical measurements. Since such a multilayered phantom will contain many more parameters, a different optical system such as the depth-sensitive multifocal color imaging system developed by our group[41] and a sequential estimation method[42] will be needed to selectively acquire color images from each layer to improve the accuracy of each estimated parameter. Although the additional melanin content could affect the color response and in turn the final estimation result, we believe that such an effect would be negligible if part of the calibration data set contains a similar melanin content. According to our previous experiment, the average relative RMSE of C_{tHb}, α and StO_2 would increase from 7.7% to 11.6% if the scattering power β was included as one free parameter instead of a known parameter. Therefore, it is expected that the average RMSE of other parameters may change in a similar trend with melanin concentration as an additional free tissue parameter. Considering the volume fraction range of melanin (1 to 3%) in the epidermis of the light skin[43] and the ratio (15%) between the epidermal thickness[44] and the typical penetration depth of our system, the total absorption coefficient of the skin may vary from 0.7 to 2.2 cm^{-1} at 550 nm due to the volume fraction variation in melanin. According to the semiempirical model,[45] the absorption coefficient variation can be converted to a decrease of around 20% in diffuse reflectance intensity at 550 nm and the same percent changes in R, G, and B color values on average. Such a decrease in the R, G, and B color values may yield an increase of about 3% in the relative RMSE according to the relationship between the effective signal to noise ratio and the relative RMSE we estimated (results not shown). Because the optical properties of phantoms were extracted mainly from Caucasians, it is recommended to create a separate calibration dataset for each different skin type, for example, skin type I-VI.[46] In this manner, the influence of color changes caused by melanin in different skin types on the proposed method will be minimized.

Besides diffuse reflectance imaging, this method can be extended to fluorescence or Raman imaging to extract the concentrations of fluorophores or Raman scatterers. Fluorescence or Raman spectral measurements can be replaced by multiple wide-band or narrow-band measurements to enhance the signal to noise ratio and speed up data acquisition. This has been demonstrated previously for spontaneous Raman spectra[31] in which the full Raman spectrum was reconstructed from multiple narrow-band measurements with small RMSEs.

5 Conclusion

In this study, we developed a method of sequential weighted WE to estimate key tissue parameters including total hemoglobin concentration (C_{tHb}), hemoglobin oxygenation (StO_2), scatterer density (α), and scattering power (β) from wide-band color measurements. Tissue phantoms with varying oxygenation were measured to evaluate this method. The estimated tissue parameters show excellent agreement with the reference values. Compared with the traditional WE, the sequential weighted WE shows significant improvement, especially for hemoglobin oxygenation. Moreover, the new method allows the estimation of the scattering properties, which overcomes the limitation of assuming known scattering properties or fixed scattering properties in the previous reports. This method is fast, thus it may allow real-time monitoring of key tissue parameters in a large tissue area when combined with color imaging. A future study will be conducted on a more complex multilayered phantom with both melanin and hemoglobin as the absorbers.

Acknowledgments

The authors would like to acknowledge financial support from the proof-of-concept grant (NRF2012NRF-POC001-015) funded by National Research Foundation as well as the public sector funding grant (122-PSF-0012) and ASTAR-ANR joint grant (102 167 0115) funded by ASTAR-SERC (Agency for Science Technology and Research, Science and Engineering Research Council) in Singapore.

References

1. Q. Liu and T. Vo-Dinh, "Spectral filtering modulation method for estimation of hemoglobin concentration and oxygenation based on a single fluorescence emission spectrum in tissue phantoms," *Med. Phys.* **36**(10), 4819–4829 (2009).
2. G. M. Palmer and N. Ramanujam, "Monte Carlo-based inverse model for calculating tissue optical properties. Part I: Theory and validation on synthetic phantoms," *Appl. Opt.* **45**(5), 1062–1071 (2006).
3. T. J. Farrell, M. S. Patterson, and B. Wilson, "A diffusion theory model of spatially resolved, steady-state diffuse reflectance for the noninvasive determination of tissue optical properties *in vivo*," *Med. Phys.* **19**(4), 879–888 (1992).
4. N. Rajaram, T. H. Nguyen, and J. W. Tunnell, "Lookup table–based inverse model for determining optical properties of turbid media," *J. Biomed. Opt.* **13**(5), 050501 (2008).
5. S. Chen and Q. Liu, "Modified Wiener estimation of diffuse reflectance spectra from RGB values by the synthesis of new colors for tissue measurements," *J. Biomed. Opt.* **17**(3), 030501 (2012).
6. S. Baronti et al., "Multispectral imaging system for the mapping of pigments in works of art by use of principal-component analysis," *Appl. Opt.* **37**(8), 1299–1309 (1998).
7. D. Anglos, C. Balas, and C. Fotakis, "Laser spectroscopic and optical imaging techniques in chemical and structural diagnostics of painted artwork," *Am. Lab.* **31**(20), 60–67 (1999).

8. C. D. Tran, "Acousto-optic tunable filter: A new generation monochromator and more," *Anal. Lett.* **33**(9), 1711–1732 (2000).
9. C. D. Tran, "Development and analytical applications of multispectral imaging techniques: An overview," *Fresen. J. Anal. Chem.* **369**(3–4), 313–319 (2001).
10. W. R. Johnson, D. W. Wilson, and G. Bearman, "All-reflective snapshot hyperspectral imager for ultraviolet and infrared applications," *Opt. Lett.* **30**(12), 1464–1466 (2005).
11. J. Hardeberg, *Acquisition, and Reproduction of Color Images: Colorimetric, and Multispectral Approaches*, PhD Dissertation, TSI Dept., ENST Bretagne, Paris (2001).
12. M. Shi and G. Healey, "Using reflectance models for color scanner calibration," *J. Opt. Soc. Am. A* **19**(4), 645–656 (2002).
13. H. Haneishi et al., "System design for accurately estimating the spectral reflectance of art paintings," *Appl. Opt.* **39**(35), 6621–6632 (2000).
14. I. Nishidate et al., "Noninvasive imaging of human skin hemodynamics using a digital red-green-blue camera," *J. Biomed. Opt.* **16**(8), 086012 (2011).
15. I. Nishidate et al., "Estimation of melanin and hemoglobin using spectral reflectance images reconstructed from a digital RGB image by the wiener estimation method," *Sensors* **13**(6), 7902–7915 (2013).
16. A. E. Cerussi et al., "Sources of absorption and scattering contrast for near-infrared optical mammography," *Acad. Radiol.* **8**(3), 211–218 (2001).
17. J. C. Ramella-Roman et al., "Polarized light imaging with a handheld camera," *Proc. SPIE* **5068**, 284–293 (2003).
18. A. N. Yaroslavsky, V. Neel, and R. R. Anderson, "Demarcation of nonmelanoma skin cancer margins in thick excisions using multispectral polarized light imaging," *J. Investig. Dermatol.* **121**(2), 259–266 (2003).
19. S. L. Jacques, J. C. Ramella-Roman, and K. Lee, "Imaging skin pathology with polarized light," *J. Biomed. Opt.* **7**(3), 329–340 (2002).
20. H. J. van Staveren et al., "Light scattering in lntralipid-10% in the wavelength range of 400–1100 nm," *Appl. Opt.* **30**(31), 4507–4514 (1991).
21. H. Dehghani et al., "Near infrared optical tomography using NIRFAST: Algorithm for numerical model and image reconstruction," *Commun. Numer. Meth. En.* **25**(6), 711–732 (2009).
22. G. Zonios and A. Dimou, "Modeling diffuse reflectance from semi-infinite turbid media: application to the study of skin optical properties," *Opt. Express* **14**(19), 8661–8674 (2006).
23. N. Doegnitz et al., "Determination of the absorption and reduced scattering coefficients of human skin and bladder by spatial frequency domain reflectometry," *Proc. SPIE* **3195**, 102–109 (1998).
24. I. V. Meglinski and S. J. Matcher, "Quantitative assessment of skin layers absorption and skin reflectance spectra simulation in the visible and near-infrared spectral regions," *Physiol. Meas.* **23**(4), 741–753 (2002).
25. A. Bashkatov et. al., "Optical properties of human skin, subcutaneous and mucous tissues in the wavelength range from 400 to 2000 nm," *J. Phys. D Appl. Phys.* **38**(15), 2543–2555 (2005).
26. E. K. Chan et. al., "Effects of compression on soft tissue optical properties," *IEEE J. Sel. Top. Quant.* **2**(4), 943–950 (1996).
27. E. Salomatina et al., "Optical properties of normal and cancerous human skin in the visible and near-infrared spectral range," *J. Biomed. Opt.* **11**(6), 064026 (2006).
28. S. A. Plowman and D. L. Smith, "Respiration," in *Exercise Physiology for Health Fitness and Performance*, pp. 279–280, Lippincott Williams & Wilkins, Baltimore, Maryland (2013).
29. G. R. Kelman, "Digital computer procedure for the conversion of PCO_2, into blood CO_2 content," *Resp. Physiol.* **3**(1), 111–115 (1967).
30. H.-W. Breuer et al., "Oxygen saturation calculation procedures: a critical analysis of six equations for the determination of oxygen saturation," *Intensive Care Med.* **15**(6), 385–389 (1989).
31. S. Chen, Y. H. Ong, and Q. Liu, "Fast reconstruction of Raman spectra from narrow-band measurements based on Wiener estimation," *J. Raman Spectrosc.* **44**(6), 875–881 (2013).
32. R. V. Lenth, "Computer intensive statistical methods: validation, model selection, and bootstrap," *Technometrics* **37**(4), 458–459 (1995).
33. D. Jakovels, U. Rubins, and J. Spigulis, "RGB imaging system for mapping and monitoring of hemoglobin distribution in skin," *Proc. SPIE* **8158**, 81580R (2011).
34. K.-H. Englmeier et al., "A method for the estimation of the hemoglobin distribution in gastroscopic images," *Int. J. Biomed. Comput.* **41**(3), 153–165 (1996).
35. S. Chen et al., "Recovery of Raman spectra with low signal-to-noise ratio using Wiener estimation," *Opt. Express* **22**(10), 12102–12114 (2014).
36. J. Khan et al., "Classification and diagnostic prediction of cancers using gene expression profiling and artificial neural networks," *Nat. Med.* **7**(6), 673–679 (2001).
37. F. Harrell, Jr., K. Lee, and D. Mark, "Multivariable prognostic models: issues in developing models, evaluating assumptions and adequacy, and measuring and reducing errors," *Stat. Med.* **15**(4), 361 (1996).
38. E. Reinhard et al., "Color transfer between images," *IEEE Comput. Graph.* **21**(5), 34–41 (2001).
39. J. E. Bender et al., "A robust Monte Carlo model for the extraction of biological absorption and scattering *in vivo*," *IEEE T. Biomed. Eng.* **56**(4), 960–968 (2009).
40. D. Yudovsky and L. Pilon, "Rapid and accurate estimation of blood saturation, melanin content, and epidermis thickness from spectral diffuse reflectance," *Appl. Opt.* **49**(10), 1707–1719 (2010).
41. C. Zhu, Y. H. Ong, and Q. Liu, "Multifocal noncontact color imaging for depth-sensitive fluorescence measurements of epithelial cancer," *Opt. Lett.* **39**(11), 3250–3253 (2014).
42. Q. Liu and N. Ramanujam, "Sequential estimation of optical properties of a two-layered epithelial tissue model from depth-resolved ultraviolet-visible diffuse reflectance spectra," *Appl. Opt.* **45**(19), 4776–4790 (2006).
43. T. Igarashi, K. Nishino, and S. K. Nayar, "The appearance of human skin: a survey," *Found. Trends Comput. Graphics Vision* **3**(1), 1–95 (2005).
44. A. E. Karsten and J. E. Smit, "Modeling and verification of melanin concentration on human skin type," *Photochem. Photobiol.* **88**(2), 469–474 (2012).
45. G. Zonios, I. Bassukas, and A. Dimou, "Comparative evaluation of two simple diffuse reflectance models for biological tissue applications," *Appl. Opt.* **47**(27), 4965–4973 (2008).
46. T. B. Fitzpatrick, "The validity and practicality of sun-reactive skin types I through VI," *Arch. Dermatol.* **124**(6), 869–871 (1988).

Shuo Chen received his bachelor's degree at Shanghai Jiaotong University in China and his master's degree at Heidelberg University in Germany. He is currently a PhD candidate at the School of Chemical and Biomedical Engineering at Nanyang Technological University in Singapore. His research is focused on fast spectroscopic imaging in biomedical applications.

Xiaoqian Lin received her bachelor's degree in optical information science and technology and her master's degree in optics from Fujian Normal University in China. She was a project officer at Nanyang Technological University from 2013 to 2014. She is currently a sales engineer in Fujian CASTECH Crystal, Inc. in China. Her research interests include surface-enhanced Raman spectroscopy, noninvasive medical diagnosis, and biomedical image processing.

Caigang Zhu received his bachelor's degree from Huazhong University of Science and Technology in China, and his PhD degree from Nanyang Technological University in Singapore. He is now a postdoctoral research fellow at the University of Washington, Seattle, in the United States. His main research interests include Monte Carlo modeling of light transport in tissue, optical spectroscopy, and imaging for cancer diagnosis.

Quan Liu received a bachelor's degree in electrical engineering from Xidian University, Xi'an, China, a master's degree in electrical engineering from the Graduate School of the University of Science and Technology of China in Beijing, China, and a PhD degree in biomedical engineering from the University of Wisconsin, Madison, USA. He is currently an assistant professor at the School of Chemical and Biomedical Engineering at Nanyang Technological University in Singapore.